Journal of Materials Chemistry A

Accepted Manuscript

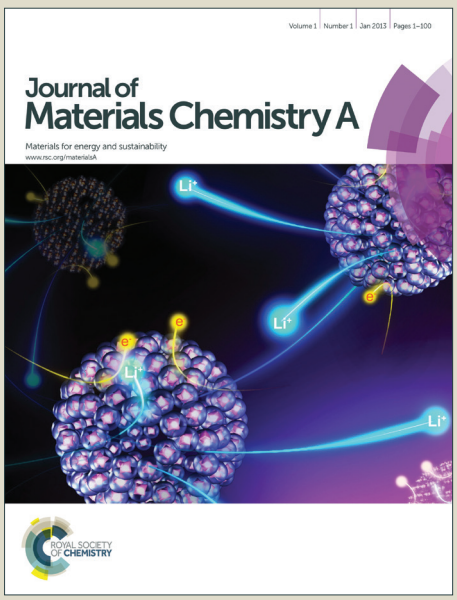

ROYAL SOCIETY OF CHEMISTRY

www.rsc.org/materialsA

Graphical Abstract

The hierarchical nanocomposites (Fe_3C@N-C) of iron carbide encaged in nitrogen-doped carbon counter electrode was fabricated for low-cost, highly efficient dye-sensitized solar cells.

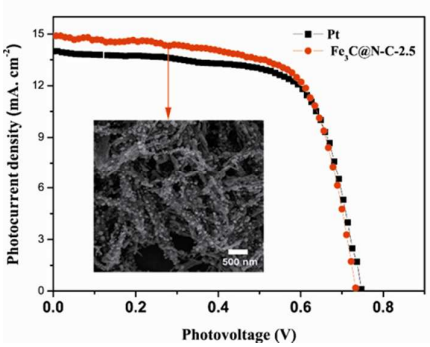

Cite this: DOI: 10.1039/c0xx00000x

www.rsc.org/xxxxxx

ARTICLE TYPE

Nitrogen-doped carbon and iron carbide nanocomposites as cost-effective counter electrodes of dye-sensitized solar cells

Hongxia Xu,‡[a] Chuanjian Zhang,‡[a] Zaiwei Wang,[ab] Shuping Pang,[a] Xinhong Zhou,*[c] Zhongyi Zhang,[a] Guanglei Cui*[a]

Received (in XXX, XXX) Xth XXXXXXXXX 20XX, Accepted Xth XXXXXXXXX 20XX
DOI: 10.1039/b000000x

The hierarchical nanocomposites of iron carbide (Fe_3C) encaged in nitrogen-doped carbon (N-C) were prepared by using a simple carbothermal reduction of iron(II) oxalate (FeC_2O_4) nanowires in the presence of cyanamide (NH_2CN) at 600 ˚C. Such Fe_3C@N-C nanocomposites delivered fair electrocatalytic activity for I_3^-/I^- redox reaction. As a result, to be explored as cost-effective counter electrodes of dye-sensitized solar cells, an efficiency of 7.36% was achieved, which was comparable to that of the cell with Pt-FTO counter electrode (7.15%) under the same experimental condition. The good electrochemical performance is attributed to synergistic effect of the combination of N-C and Fe_3C and one dimentional configuration, which endow the nanocomposites more interfacial active sites and improved electron transfer efficiency for the reduction of I_3^-/I^-.

Introduction

Nanocrystalline dye-sensitized solar cells (DSSCs), introduced by Grätzel and O'Regan in 1991, have attracted considerable attention from academic and industrial field because of cost effectiveness and comparable high light-to-electricity conversion efficiency (η) and ease of manufacturing.[1-6] The counter electrodes (CE), as one of essential components of the DSSCs, are usually composed of the noble metal platinum (Pt) coated on the transparent conductive oxides (such as indium-doped tin oxide). However, the limited supply and the high cost of Pt hinder their large-scale commercial applications in DSSCs counter electrode.[7,8] Therefore, it is imperative to develop low-cost, abundant and highly-efficient substitutes for the conventional Pt counter electrode in the DSSCs system. Many materials such as carbon materials,[5,9-12] conductive polymers,[13,14] inorganic materials including metal nitrides,[15-17] carbides,[18,19] sulfides[20-23] and selenide[24,25] and composites have been employed to replace Pt as CE in DSSCs.

Among these counter electrode materials, transition metal carbides, such as Molybdenum, Tungsten, Niobium and Vanadium,[18,19] have been shown to have good catalytic activity for the reduction of triiodide to iodide in DSSCs. However, these metal carbides contain rare earth elements. Iron carbide (Fe_3C) seems more attractive for its abundance in the earth's crust and its high electronic conduction, higher resistance against oxidation and good catalytic activity[26] as well. However, iron carbide (Fe_3C) has been less investigated in DSSCs mainly because of the preconception that iron carbide is metastable compound, which readily decomposes into α-Fe and carbon.[27] Moreover, α-Fe is susceptible to corrosion by I^-/I_3^- redox species.[28] Very recently, Fu *et al.* found that the Fe_3C could survive very well in I^-/I_3^- electrolyte and fair efficiency of 6.04% was obtained. However, as mentioned in this work, α-Fe is coexisted in the compound and an additional etching process is required to remove the unstable α-Fe.[29]

As the counter electrode of DSSCs, the electronic conductivity is as equally important as the catalytic activity to decrease the overvoltage to minimize the energy losses.[30] It is known that catalytic and electronic properties of transition metal compounds are governed by their intrinsic materials. However, Bulk materials usually exhibit limited catalytic activity probably because of their large particle size and less specific surface area.[31] Nanostructure materials have been known to show better properties compared to their corresponding bulk materials. Therefore, it is great significance to further explore high efficient counter electrode of transition metal compounds by rational design of nanostructured catalytic materials. Among different kinds of nanoscale morphologies, one-dimensional nanostructure is known to be beneficial for electronic conduction along the axial direction.[22] Herein, iorn carbide encaged in nitrogen-doped carbon (Fe_3C@N-C) nanowires were synthesized by directly annealing of iron(II) oxalate (FeC_2O_4) nanowires in H_2 atmosphere with cyanamide (NH_2CN) as the structure confinement agent. At optimized annealing temperature, the composites with varied Fe_3C concentration were explored as the counter electrode in DSSCs. Because of synergetic effect of N-C and Fe_3C, and the presence of one dimentional morphology, Fe_3C@N-C-2.5 (ratio of FeC_2O_4/CH_2N_2 is 2.5) nanostructures as counter electrodes exhibited comparable photovoltaic performance compared with those of Pt-FTO.

Experimental

Materials

Cetyltrimethylammonium bromide (CTAB), Iron(Ⅱ) chloride tetrahydrate ($FeCl_2{\cdot}4H_2O$), andoxalic acid ($H_2C_2O_4$) were purchased from Sinopharm Chemical Reagent Co., Ltd., China. Iodine and 4-tert-butylpyridine were purchased form TCI. N719 dye ($Ru(dcbpy)_2(NCS)_2$, (dcbpy = 2,2-bipyridyl-4,4-dicarboxylato)) was purchased from Solaronix SA. TiO_2 paste and 1,2-dimethyl-3-propylimidazolium iodide were purchased from Wuhan GeAo Tech Co., Ltd., China. Guanidinium thiocyannate was purchased from Dalian HeptaChroma Solar Tech Co., Ltd., China. All the chemicals are analytical grade without further purification.

Synthesis of Fe_3C@N-C

FeC_2O_4 nanowires were firstly synthesized as precursor of Fe_3C product via a microemulsion route. 10 g CTAB which served as soft template was added to a mixture of cyclohexane (300 mL) and n-pentanol (10 mL). After stirring for 30 min, 15 mL of 1 M $H_2C_2O_4$ and 5 mL of 1 M $FeCl_2{\cdot}4H_2O$ aqueous solution was added to the above microemulsion and stirred for another 24 hrs at ambient temperature. The yellow precipitate was filtered and washed with ethanol to remove the impurity.[32] After dried overnight in a vacuum oven at 50˚C, the as-synthesized FeC_2O_4 nanowires was dispersed in ethanol which contained a certain amount of NH_2CN for homogenous precursor mixing before heat treatment. After dried again, the mixed raw powders were annealed at various temperatures for 2 hrs under hydrogen atmosphere and the black Fe_3C@N-C nanocomposites were finally obtained. The obtained Fe_3C@N-C nanocomposites with the weight ratio of FeC_2O_4/ NH_2CN of 1, 2.5, 4 were labeled as Fe_3C@N-C-1, Fe_3C@N-C-2.5, Fe_3C@N-C-4.

Preparation of counter electrodes

The mirror-like Pt/FTO electrode was obtained by electrodepositing a platinum layer on the surface of fluorine-doped tin oxide substrate. The thickness of Pt films is about 75 nm. The Fe_3C@N-C (30 mg) and polyvinylidene fluoride dissolved in N-methyl-2-pyrrolidinone (10%, wt.%) were grinded together to generate homogenous paste. Subsequently, the counter electrode films were prepared on precleaned fluorine-doped tin oxide (FTO) substrate by doctor blade technique followed by heat drying at 60 ˚C for 24 hrs.

Fabrication of DSSCs

TiO_2 working photoanodes were prepared on FTO substrate using TiO_2 pastes by doctor blade technique and subsequently sintered at 500 ˚C for 30 min in air. The resultant TiO_2 photoanodes were soaked in an ethanol solution of N719 dye (3×10^{-4} M) for 24 hrs to obtain dye-sensitized TiO_2 electrode. The dye-adsorbed TiO_2 photoanodes with an active area of 0.16 cm^2 were assembled with Fe_3C@N-Cand platinum counter electrodes using laboratory tape as a spacer to fabricate corresponding sandwich-type cells, respectively. The liquid electrolyte is composed of 0.6 M 1,2-dimethyl-3-propylimidazolium iodide (DMPII), 0.03 M iodine (I_2), 0.06 M lithium iodide (LiI), 0.5 M 4-*tert*-butylpyridine (TBP), and0.1 M guanidinium thiocyannate with acetonitrile (ACN) as the solvent.

Characterization

The morphologies of Fe_3C@N-C were investigated using field emission scanning electron microscopy (FESEM, HITACHI S-4800), and high-resolution transmission electron microscopy (HRTEM, JEOL 2010F). X-ray diffraction (XRD) patterns were recorded with a Bruker-AXS Micro-diffractometer (D8 ADVANCE) using Cu Kα radiation (λ = 1.5406 Å) from 20 ˚C to 70 ˚C. Cyclic voltammetry (CV) was carried out in a three-electrode system in an acetonitrile solution of 0.1 M $LiClO_4$, 10 mM LiI, and 1 mM I_2. Platinum served as a counter electrode and the non-aqueous Ag/Ag^+ couple was applied as a reference electrode. The photocurrent-voltage characteristics of the DSSCs were measured with a Newport (USA) solar simulator (300 W Xe source) and a Keithley 2440 source meter. Electrochemical impedance spectroscopy (EIS) measurements were performed using a Zahner Zennium electrochemical workstation by applying an AC voltage of 10 mV amplitude in the frequency range between 100 kHz and 100 mHz at room temperature. Fitting of impedance spectra to the proposed equivalent circuit was performed by using the Zview software.

Result and discussion

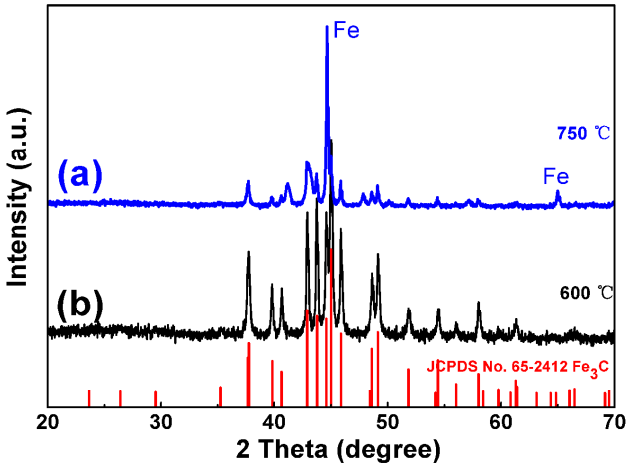

Fig. 1 Typical XRD patterns of Fe_3C samples synthesized at 750 ˚C and 600 ˚C.

Fig. 1 depicts the XRD patterns of Fe_3C samples (Fe_3C@N-C-2.5) synthesized at 600 ˚C and 750 ˚C when the weight ratio of FeC_2O_4/ NH_2CN is 2.5 (R = 2.5). After annealed at 600 ˚C，all the peaks of the sample could be indexed to orthorhombic Fe_3C (JCPDS No. 65-2412) without any impurity phase which has been shown in Fig. 1(b). However, when the reaction temperature was raised to 750 ˚C, two peaks corresponding to α-Fe were detected and shown in Fig. 1(a). This is consistent with the previously reported results that the decomposition of Fe_3C into α-Fe and carbon occurred at T > 600 ˚C.[27] No diffraction peaks of graphite were observed which implied that the carbon component in the composites was amorphous due to the low annealed temperature. In order to avoid the generation of α-Fe which suffers from chemical instability in I^-/I_3^- electrolyte, the optimized reaction temperature was 600 ˚C. The influence of FeC_2O_4/ NH_2CN ratio on product composition was also evaluated at the optimized temperature. As shown in Fig. S1, both the patterns exhibited Fe_3C phase which coincide with the sample obtained at R = 2.5 (Fig. 1(b)). This implied that the FeC_2O_4/NH_2CN ratio may only change the relative amount of

Fe_3C and carbon but does not affect the crystal structure of Fe_3C in final product. The element analysis results shown in Table S1 indicated as-synthesized Fe_3C sample comprised of C, N, Fe. It is reported that NH_2CN was condensed to C_3N_4 and decomposed into N-doped carbon(C-N) at high temperature.[33] Therefore, Fe_3C sample was the composite of Fe_3C and minor amount of N-doped carbon. Meanwhile, the element analysis results indicated that with an increasing FeC_2O_4/NH_2CN ratio, the content of Fe_3Cincreased correspondingly in the as-prepared product.

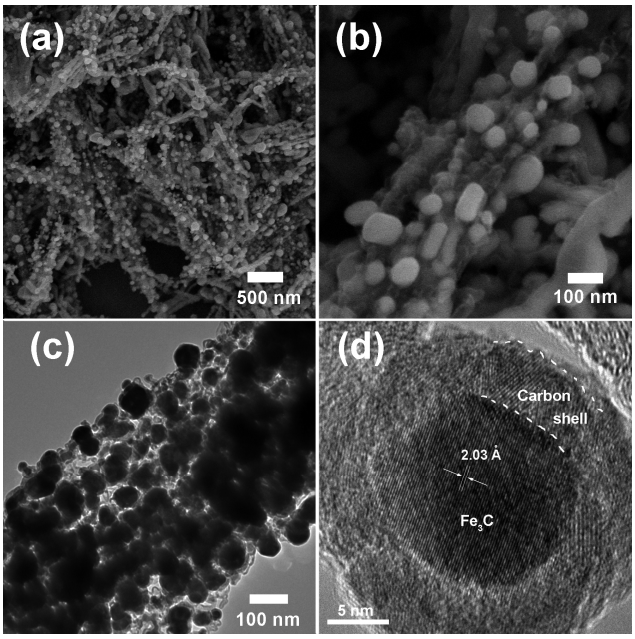

Fig. 2 Typical SEM and its enlarged images (a, b), TEM (c) and HRTEM (d) images of Fe_3C@N-C-2.5.

Typical SEM and TEM images of as-synthesized FeC_2O_4 are shown in Fig. S2. It can be clearly seen that the obtained FeC_2O_4 exhibits one dimentional nanowire morphology and relatively smooth surface. After reacted with NH_2CN (R=2.5), chain-like Fe_3C@N-C nanomaterials were observed in Fig. 2(a) and most of the composites maintained the one dimensional morphology. This may be due to the appropriate amount of NH_2CN (R = 2.5) addition which could prevent nanowires from aggregation. When the FeC_2O_4/NH_2CN ratio was varied to 1 as shown in Fig. S3 (a) and (b), most of the Fe_3C nanowires displayed a rod-like aggregation structure which may be unfavorable to electronic transportation. When the FeC_2O_4/NH_2CN ratio was raised to 4, Fe_3C with minor carbon coating were observed which are shown in Fig. S3 (c) and (d), where well electronic-connection is difficult to be achieved between isolated Fe_3C nanoparticles. However, from the enlarged micrographs shown in Fig. 2(b) and 2(c), Fe_3C nanoparticles with size below 100 nm were well connected together by N-doped carbon at R=2.5. This unique structure is expected to be beneficial to the electron transfer during catalytic reaction. HRTEM given in Fig. 2 (d) confirmed that Fe_3C nanoparticle was well encapsuled by a N-doped carbon layer with the fringe spacing of 2.03 Å corresponding to the (112) planes of orthorhombic Fe_3C.[34] In addition, elemental mapping in Fig. S4 elucidated that Fe, C and N were homogenously distributed in composites. The much narrower D and G peak width in Fig. S5 implied that the carbon of Fe_3C@N-C-2.5 was more crystalline than that of Fe_3C@N-C-1. From the above results, well-wired Fe_3C nanoparticles, as well as the carbon sheath in Fe_3C@N-Cnanocomposite may expect to present wonderful catalytic activity when used as CE in DSSCs.

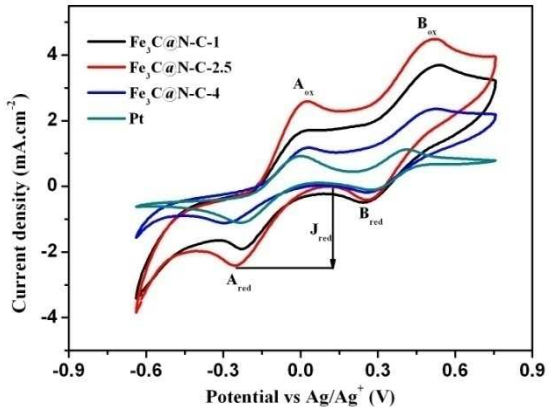

Fig. 3 CaptionCyclic voltammograms of Pt, Fe_3C@N-C counter electrodes with different raw materials ratio in 10 mM LiI, 1 mM I_2 and 0.1 M $LiClO_4$ acetonitrile solution at a scan rate of 20 mV s^{-1}.

Cyclic voltammetry (CV) was performed to evaluate the electrocatalytic activity of counter electrodes to reduce triiodide using a three-electrode system. CV curves for I_3^-/I^- redox reaction obtained on Fe_3C@N-C and the reference Pt counter electrodes at a scan rate of 20 mV s^{-1} are shown in Fig. 3. Counter electrodes with good electrocatalytic activity for I_3^-/I^- electrolyte display two typical pairs of redox peaks, A_{ox}/A_{red} and B_{ox}/B_{red}. The A_{ox}/A_{red} is assigned to the redox reaction shown in Eq. (1) and B_{ox}/B_{red} is ascribed to redox reaction shown in Eq. (2).[35] From Fig. 3, it can be seen the CV curves of the CEs with Fe_3C@N-C displayed two pairs of redox peaks, indicating that they all possess electrocatalytic ability for the reduction of triiodide ions. A higher reduction peak current density (J_{red}) and a lower peak-to-peak voltage separation (V_{PP}) indicate a better catalytic activity. The redox peaks (A_{ox} and A_{red}) directly affects the DSSC performance. Therefore, we focused on investigation about peak current density (J_{red}) and peak-to-peak voltage separation (V_{PP}) of A_{ox} and A_{red}. The profile and location of the A_{ox} and A_{red} redox peaks of Fe_3C@N-C CEs were close to those of Pt CE. This indicated Fe_3C@N-C CEs and Pt CE possessed similar E_{pp} value. However, the cathodic current density increased in the order of Fe_3C@N-C-4 (1.15 mA cm^{-2}) < Pt(1.21 mA cm^{-2}) < Fe_3C@N-C-1 (1.68mA cm^{-2})< Fe_3C@N-C-2.5 (2.41mA cm^{-2}). By comprehensive consideration of the E_{pp} and peak current density, the Fe_3C@N-C-2.5 presented slightly closer E_{pp} but much larger cathodic current density than that of the Pt CE, demonstrating a relatively better electrocatalytic activity than that of the Pt CE. The enhanced electrocatalytic activity can be attributed to synergistic effect of the combination of high catalytic activity and good electrical conductivity of nitrogen-doped carbon into Fe_3C and the morphology of nanowires which is beneficial to electron transfer.[36] Fig. S6 shows a 100-cycles CVs for Fe_3C@N-C-2.5 electrode at a scan rate of 20 mV s^{-1}. They present almost unchanged curves shape and constant redox peak current densities, indicating an comparable electrochemical stability of the Fe_3C@N-C-2.5 CE.

$$I_3^- + 2e^- \rightleftharpoons 3I^- \quad (1)$$

$$3I_2 + 2e^- \rightleftharpoons 2I_3^- \quad (2)$$

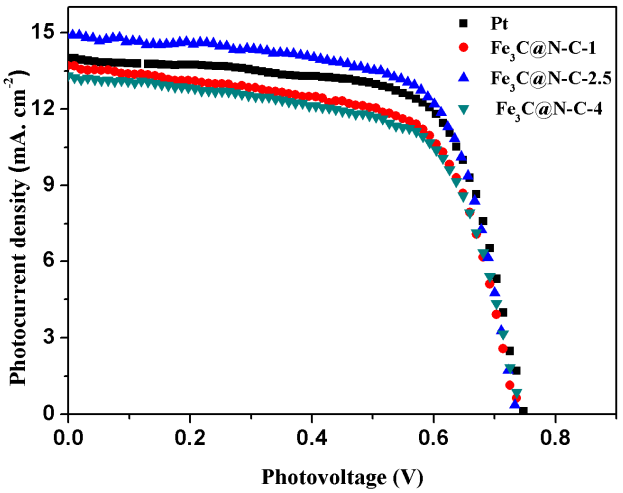

Fig. 4 Characteristic photocurrent density-voltage (*J-V*) curves of DSSCs with different electrodes, measured under simulated sunlight 100 mW cm^{-2} (AM 1.5). The liquid electrolyte is composed of 0.6 M 1,2-dimethyl-3-propylimidazolium iodide (DMPII), 0.03 M iodine (I_2), 0.06 M lithium iodide (LiI), 0.5 M 4-*tert*-butylpyridine (TBP), and0.1 M guanidinium thiocyannate in acetonitrile solution.

The photocurrent density-voltage (*J-V*) characteristic curves of the DSSCs fabricated with different counter electrodes measured under the illumination of 1 sun (100 mW cm^{-2}) are shown in Fig. 4. The photovoltaic parameters of these devices, including the short-circuit current (J_{sc}), the open-circuit voltage (V_{oc}), the fill factor (FF), and the energy conversion efficiency (η), are summarized in Table 1. All devices, with the CEs containing Fe_3C, had similar V_{oc}. However, J_{sc} (FF) complied with the order Fe_3C@N-C-2.5 >Pt >Fe_3C@N-C-1 >Fe_3C@N-C-4. This is in accordance with the results of CVs measurements. The DSSCs with Fe_3C@N-C counter electrodes exhibited a relatively higher η. The Fe_3C@N-C-1, Fe_3C@N-C-2.5, and Fe_3C@N-C-4 give η of 6.52%, 7.36%, and 6.36%, respectively. The DSSCs with Fe_3C@N-C-2.5 CE possessed the best energy conversion efficiencies of 7.36% which was comparable with that of the DSSCs with Pt CE (7.15%).

Table 1 Characteristics of the *J-V* curves of the DSSCs fabricated using different counter electrodes

Counter Electrode	J_{sc}(mA/cm^2)	V_{oc} (mV)	FF(%)	η (%)
Fe_3C@N-C-1	13.74	738	64.31	6.52 ± 0.04
Fe_3C@N-C-2.5	14.97	741	66.35	7.36 ± 0.03
Fe_3C@N-C-4	13.39	741	64.08	6.36 ± 0.04
Pt	14.13	747	67.71	7.15 ± 0.02

[a] V_{oc}: open circuit voltage, J_{sc}: short circuit current density, FF: fill factor, η: energy conversion efficiency.

In order to further evaluate the electrochemical activity of the composite materials as counter electrodes in DSSCs, the electrochemical impedance spectra (EIS) were measured in a symmetric sandwich cell configuration consisting of two identical counter electrodes. Their Nyquist plots are illustrated in Fig. 5. For comparison, the impedance spectrum of the cell consisting of the conventional platinized electrodes was also presented here.

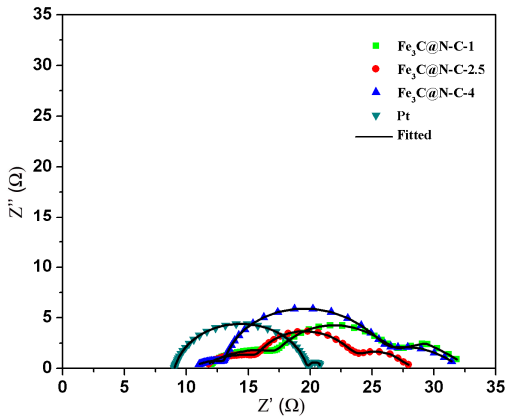

Fig. 5 Nyquist plots for the symmetric cells fabricated with two identical counter electrodes of Fe_3C@ N-C-1 (■), Fe_3C@ N-C-2.5 (●), Fe_3C@ N-C-4 (▲), Pt (▼). The lines express fit results for corresponding EIS data. The cells were measured with the frequency range between 100 kHz and 100 mHz.

Table 2 EIS parameters of the symmetric cells based on different counter electrodes

Counter Electrode	R_s (Ω)	R_{ct}(Ω)	$R_{ct}(S)$(Ω)
Fe_3C@N-C-1	10.9	7.77	7.10
Fe_3C@N-C-2.5	10.75	6.78	5.58
Fe_3C@N-C-4	10.38	12.3	2.83
Pt	9.04	10.65	~

[a] R_s: series resistance, R_{ct}: charge-transfer resistance, $R_{ct}(S)$: impedance arising from the Fe_3C@N-C-FTO interface

For a conventional symmetric cell consisting of platinized electrodes, the electric circuit elements should have a series resistance (R_s), a constant phase element (CPE), the charge transfer resistance (R_{ct}) and Nernst diffusion impedance of the I_3^-/I^- redox species within a thin layer in the electrolyte.[37] However, for a symmetric cell based on Fe_3C@N-C electrodes, three semicircles were visible for Fe_3C@N-C compared with two semicircle of the conventional Pt. The semicircle in the high frequency region was speculated to correspond to impedance arising from the Fe_3C@N-C-FTO interface ($R_{ct}(S)$)[38]. The one in the middle frequency region is associated with the charge-transfer resistance of counter electrode/redox (I^-/I_3^-) interface and the capacitance of the counter electrode/electrolyte interface. The low-frequency semicircle is attributed to Nernst diffusion impedance of the I_3^-/I^- redox species within a thin layer in the electrolyte. The intercept of the real axis at high frequency represents the ohmic series resistance including the sheet resistance of two identical CEs and the electrolytic resistance. The equivalent circuit is given in the Fig. S7 and the simulated data from the EIS spectra for Fe_3C@N-C and Pt are summarized in Table 2. The Fe_3C@N-C CEs had slightly larger R_s than Pt CE (Table 2), indicating that Fe_3C@N-C had relatively lower conductivity compared with Pt. The impedance arising from the Fe_3C@N-C-FTO interface of Fe_3C@N-C-1, Fe_3C@N-C-2.5 and Fe_3C@N-C-4 are 7.10 Ω, 5.58 Ω, and 2.83 Ω. The results demonstrated that bonding strength between Fe_3C@N-C and FTO became stronger with the increase of content of Fe_3C. The simulated charge-transfer resistances of Fe_3C@N-C-1, Fe_3C@N-C-2.5, and Fe_3C@N-C-4 counter electrode are 7.77 Ω, 6.78 Ω, and 12.3 Ω respectively. The charge-transfer resistances

Fe_3C@N-C-1 and Fe_3C@N-C-2.5 are much lower than that of Pt electrode (10.65 Ω), suggesting the higher electrocatalytic activity of Fe_3C@N-C electrodes over Pt-FTO electrode for the reduction of triiodide ions. The charge-transfer resistance of Fe_3C@N-C-2.5 is much lower than that of other Fe_3C@N-C electrode which may be attributed to efficient electrocatalytic activity from the optimal interaction between the Fe_3C and carbon and enhanced electron transport capability contributed by the nanowire morphology.[36] The enhanced charge-transfer resistance of Fe_3C@N-C-4 may be due to decreased content of carbon which decreased electrocatalytic activity of Fe_3C@N-C composites. The EIS results agree with the CV data. The lower resistance would endow a greater FF and higher η in solar cell which is corrugated by the corresponding performance measurement.

Conclusions

In summary, N-C and Fe_3C nanocomposite (Fe_3C@N-C) was fabricated by carbothermal reduction using cyanamide as nitrogen and carbon source. Appropriate amount of NH_2CN prevented FeC_2O_4 nanowires aggregation and generated a favorable carbon-coating at 600 ˚C. Dye-sensitized solar cells with Fe_3C@N-C nanocomposite films as the counter electrode were explored. Among these DSSCs fabricated from Fe_3C@N-C, Fe_3C@N-C-2.5 yielded the highest photoelectrical conversion efficiency of 7.36%. That is because that the synergetic combination of the N-doped carbon and Fe_3C, generating better catalytic performance and lowest charge-transfer resistance. Moreover, Fe_3C@N-C-2.5 nanowire configuration is favorable for fast electron transfer. The abundance of Fe element and facile synthesis method endowed Fe_3C-based nanocomposites promising candidate of large-scale, highly efficient and low-cost counter electrode for DSSCs.

Acknowledgements

This work was supported by National Program on Key Basic Research Project of China (973 Program) (No. MOST2011CB935700), the National Natural Science Foundation (Grant No. 21202178, 21271180), the Shandong Province Natural Science Foundation (Grant No. ZR2011BQ024, ZR2013FZ001 and ZR2010BM016).

Notes and references

[a]*The Qingdao Key Lab of solar energy utilization and energy storage technology, Qingdao Institute of Bioenergy and Bioprocess Technology, Chinese Academy of Sciences, Qingdao, 266101, P. R. China. Fax: +8653280662744; Tel: +8653280662746; E-mail:cuigl@qibebt.ac.cn*
[b]*University of Chinese Academy of Sciences, Beijing, 100049, P. R. China*
[c]*Qingdao University of Science and Technology, Qingdao, 266101, P. R. China*

† Electronic Supplementary Information (ESI) available: XRD patterns of Fe_3C@N-C nanocomposites with different FeC_2O_4/NH_2CN ratio, Element analysis results of Fe_3C@N-C with different R value, SEM and TEM images of FeC_2O_4, TEM images of Fe_3C@N-C-1 and Fe_3C@N-C-4, Elemental mapping of Fe_3C@N-C nanocomposites, Raman spectra of Fe_3C@N-C-1, Fe_3C@N-C-2.5, Consecutive 100 cyclic voltammograms for the Fe_3C@N-C-2.5 CE, equivalent circuits for the symmetric cells consisted of platinum electrodes (a) Fe_3C@N-C (b), SEM images of nearly pure N-C and non-1D configuration Fe_3C@N-C-2.5 and Characteristics of the J-V curves of the DSSCs fabricated using nearly pure N-C and non-1D configuration Fe_3C@N-C-2.5. See DOI: 10.1039/b000000x/

‡ These authors contributed equally to this work.

1 B. O'Regan and M. Grätzel, *Nature*, 1991**, 353**, 737-740.
2 M. Grätzel, *Nature*, 2001, **414**, 338-344.
3 L. M. Peter, *Phys. Chem. Chem. Phys.*, 2007, **9**, 2630-2642.
4 N. Yang, J. Zhai, D. Wang, Y. Chen and L. Jiang, *ACS Nano*, 2010, **4**, 887-894.
5 X. Wang, L. Zhi and K. Müellen, *Nano Lett.*, 2007, **8**, 323-327.
6 J. Wang and Z. Lin, *Chem. – Asian J.*, 2012, **7**, 2754-2762.
7 N. Papageorgiou, *Coord. Chem. Rev.*, 2004, **248**, 1421-1446.
8 E. Olsen, G. Hagen and S. Eric Lindquist, *Sol. Energy Mater. Sol. Cells*, 2000, **63**, 267-273.
9 H. Wang, K. Sun, F. Tao, D. J. Stacchiola and Y. H. Hu, *Angew. Chem. Int. Ed.*, 2013, **52**, 9210-9214.
10 M. Wu, X. Lin, T. Wang, J. Qiu and T. Ma, *Energy Environ. Sci.*, 2011, **4**, 2308-2315.
11 Z. Yang, M. Liu, C. Zhang, W. W. Tjiu, T. Liu and H. Peng, *Angew. Chem. Int. Ed.*, 2013, **52**, 3996-3999.
12 H. Wang and Y. H. Hu, *Energy Environ. Sci.*, 2012, **5**, 8182-8188.
13 H. Wang, Q. Feng, F. Gong, Y. Li, G. Zhou and Z.-S. Wang, *J. Mater. Chem. A*, 2013, **1**, 97-104.
14 (a) Q. Tai, B. Chen, F. Guo, S. Xu, H. Hu, B. Sebo and X.-Z. Zhao, *ACS Nano*, 2011, **5**, 3795-3799. (b) T.-L. Zhang, H.-Y. Chen, C.-Y. Su and D.-B. Kuang, *J. Mater. Chem. A*, 2013, **1**, 1724-1730.
15 Q. W. Jiang, G. R. Li and X. P. Gao, *Chem. Commun.*, 2009, 6720-6722.
16 M. Wu, Q. Zhang, J. Xiao, C. Ma, X. Lin, C. Miao, Y. He, Y. Gao, A. Hagfeldt and T. Ma, *J. Mater. Chem.*, 2011, **21**, 10761-10766.
17 X. Zhang, X. Chen, S. Dong, Z. Liu, X. Zhou, J. Yao, S. Pang, H. Xu, Z. Zhang, L. Li and G. Cui, *J. Mater. Chem.*, 2012, **22**, 6067-6071.
18 M. Wu, X. Lin, A. Hagfeldt and T. Ma, *Angew. Chem. Int. Ed.*, 2011, **50**, 3520-3524.
19 M. Wu, X. Lin, Y. Wang, L. Wang, W. Guo, D. Qi, X. Peng, A. Hagfeldt, M. Grätzel and T. Ma, *J. Am. Chem. Soc.*, 2012, **134**, 3419-3428.
20 M. Wang, A. M. Anghel, B. Marsan, N.-L. Cevey Ha, N. Pootrakulchote, S. M. Zakeeruddin and M. Grätzel, *J. Am. Chem. Soc.*, 2009, **131**, 15976-15977.
21 Z. Ku, X. Li, G. Liu, H. Wang, Y. Rong, M. Xu, L. Liu, M. Hu, Y. Yang and H. Han, *J. Mater. Chem. A*, 2013, **1**, 237-240.
22 C.-W. Kung, H.-W. Chen, C.-Y. Lin, K.-C. Huang, R. Vittal and K.-C. Ho, *ACS Nano*, 2012, **6**, 7016-7025.
23 X. Xin, M. He, W. Han, J. Jung and Z. Lin, *Angew. Chem. Int. Ed.*, 2011, **50**, 11739-11742.
24 F. Gong, H. Wang, X. Xu, G. Zhou and Z.-S. Wang, *J. Am. Chem. Soc.*, 2012, **134**, 10953-10958.
25 (a) Z. Zhang, S. Pang, H. Xu, Z. Yang, X. Zhang, Z. Liu, Z. Wang, X. Zhou, S. Dong, X. Chen, L. Gu and G. Cui, *RSC Adv.*, 2013, **3**, 16528-16533. (b) F. Gong, X. Xu, Z. Li, G. Zhou and Z.-S. Wang, *Chem. Commun.*, 2013, **49**, 1437-1439.
26 Z. Wen, S. Ci, F. Zhang, X. Feng, S. Cui, S. Mao, S. Luo, Z. He and J. Chen, *Adv. Mater.*, 2012, **24**, 1399-1404.
27 C. Giordano, A. Kraupner, I. Fleischer, C. Henrich, G. Klingelhofer and M. Antonietti, *J. Mater. Chem.*, 2011, **21**, 16963-16967.
28 J. C. G. Wren, G. A.; Merritt, J., *J. Nucl. Mater.*, 1999, **265**, 161-177.
29 Y. Liao, K. Pan, L. Wang, Q. Pan, W. Zhou, X. Miao, B. Jiang, C. Tian, G. Tian, G. Wang and H. Fu, *ACS Appl. Mater. Interfaces*, 2013, **5**, 3663-3670.
30 J. Halme, M. Toivola, A. Tolvanen and P. Lund, *Sol. Energy Mater. Sol. Cells*, 2006, **90**, 872-886.
31 J. Qi, L. Jiang, Q. Jiang, S. Wang and G. Sun, *J. Phys. Chem. C*, 2010, **114**, 18159-18166.
32 N. Du, Y. Xu, H. Zhang, C. Zhai and D. Yang, *Nanoscale Res. Lett.*, 2010, **5**, 1295 - 1300.
33 Y.-S. Jun, W. H. Hong, M. Antonietti and A. Thomas, *Adv. Mater.*, 2009, **21**, 4270-4274.
34 Q. Su, J. Li, G. Du and B. Xu, *J. Phys. Chem. C*, 2012, **116**, 23175-23179.

35 A. I. Popov and D. H. Geske, *J. Am. Chem. Soc.*, 1958, **80**, 1340-1352.

36 (a) J. Song, G. R. Li, F. Y. Xiong and X. P. Gao, *J. Mater. Chem.*, 2012, **22**, 20580-20585. (b) G.-r. Li, F. Wang, Q.-w. Jiang, X.-p. Gao and P.-w. Shen, *Angew. Chem. Int. Ed.*, 2010, **49**, 3653-3656.

37 F. Fabregat-Santiago, J. Bisquert, E. Palomares, L. Otero, D. Kuang, S. M. Zakeeruddin and M. Grätzel, *J. Phys. Chem. C*, 2007, **111**, 6550-6560.

38 (a) T. N. Murakami, S. Ito, Q. Wang, M. K. Nazeeruddin, T. Bessho, I. Cesar, P. Liska, R. Humphry-Baker, P. Comte, P. t. Péchy and M. Graïtzel, *J. Electrochem. Soc.*, 2006, **153**, A2255-A2261. (b) P. Joshi, Z. Zhou, P. Poudel, A. Thapa, X.-F. Wu and Q. Qiao, *Nanoscale*, 2012, **4**, 5659-5664.